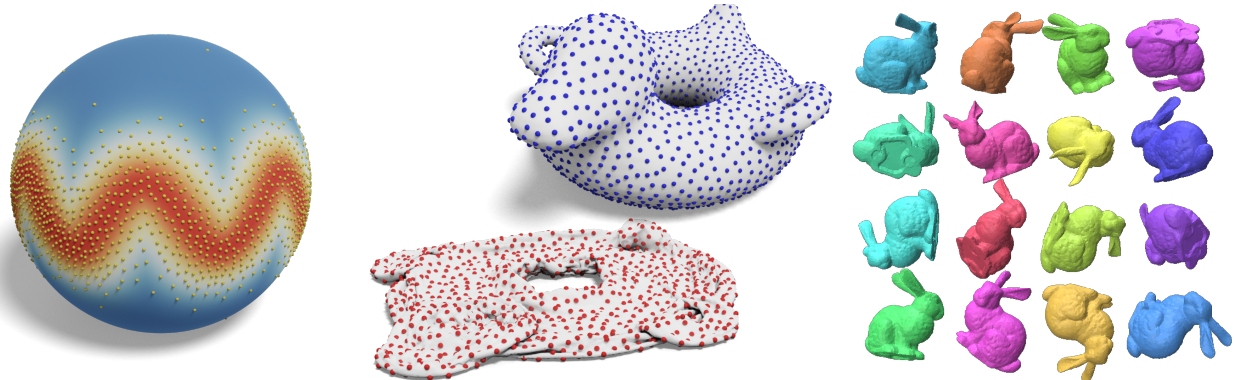


# Non-Euclidean Sliced Optimal Transport Sampling

Baptiste Genest<sup>1</sup> , Nicolas Courty<sup>2</sup>  and David Coeurjolly<sup>1</sup> 

<sup>1</sup>Univ Lyon, CNRS, Lyon1, INSA, LIRIS, France

<sup>2</sup>Université Bretagne Sud, IRISA, CNRS, France



**Figure 1:** We propose a new technique to generate well-dispersed samples on non-Euclidean domains (spherical, hyperbolic and projective spaces) using an extension of the sliced optimal transport sampling. As an example, this allows us to sample probability measures on the high-dimensional sphere (left). Using the uniformization theorem to conformally embed discrete manifolds to spherical or hyperbolic spaces, we can also generate blue noise samples in a purely intrinsic manner (red samples on the flatten geometry that exhibits blue noise properties when mapped back to a better embedding in  $\mathbb{R}^3$  in blue). Finally, we also demonstrate that such an approach can be used to blue noise sample unit quaternions (hence rotations) on the projective space of dimension 3 (right).

## Abstract

In machine learning and computer graphics, a fundamental task is the approximation of a probability density function through a well-dispersed collection of samples. Providing a formal metric for measuring the distance between probability measures on general spaces, Optimal Transport (OT) emerges as a pivotal theoretical framework within this context. However, the associated computational burden is prohibitive in most real-world scenarios. Leveraging the simple structure of OT in 1D, Sliced Optimal Transport (SOT) has appeared as an efficient alternative to generate samples in Euclidean spaces. This paper pushes the boundaries of SOT utilization in computational geometry problems by extending its application to sample densities residing on more diverse mathematical domains, including the spherical space  $\mathbb{S}^d$ , the hyperbolic plane  $\mathbb{H}^d$ , and the real projective plane  $\mathbb{P}^d$ . Moreover, it ensures the quality of these samples by achieving a blue noise characteristic, regardless of the dimensionality involved. The robustness of our approach is highlighted through its application to various geometry processing tasks, such as the intrinsic blue noise sampling of meshes, as well as the sampling of directions and rotations. These applications collectively underscore the efficacy of our methodology.

## CCS Concepts

- Computing methodologies → Computer graphics;

## 1. Introduction

2 In recent years, Optimal Transport has become a key mathematical  
3 framework for manipulating generalized probability density func-

4 tions (e.g. [V\*09]). The most general way to describe the interest  
5 of OT is that it allows quantifying meaningfully how costly it is  
6 to move masses from a generalized probability density function  
7 to another one. This defines a natural notion of distance between

8 probability measures, the Wasserstein distance, allowing the design  
 9 of displacement interpolations between measures or when dealing  
 10 with more than two measures, the notion of Wasserstein barycenter.

11 The high versatility of the framework and the numerous developments  
 12 of efficient numerical solvers make the OT become standard  
 13 in many machine learning [HGK<sup>\*</sup>16, CTR16, ACB17], computer  
 14 vision, or computer graphics applications [DGBOD12, SRGB14,  
 15 SdGP<sup>\*</sup>15, BRPP15, QCHC17, NG18, BC19, PBC<sup>\*</sup>20, SGSS22] (see  
 16 [BD23] for a recent survey).

17 Among computer graphics applications, OT has become a  
 18 widely spread tool for point pattern design and Monte Carlo in-  
 19 tegration [QCHC17, PBC<sup>\*</sup>20, SGSS22]. The main argument is  
 20 that OT offers a mathematical framework to characterize well-  
 21 distributed, or blue noise, samples in a domain leading to an ef-  
 22 ficient Monte Carlo integration or signal reconstruction [SÖA<sup>\*</sup>19].  
 23 This can be achieved by optimizing the samples positions such that  
 24 the Wasserstein distance to the uniform measure in the domain is  
 25 minimized. More recently, OT on non-Euclidean spaces has been  
 26 developed in the machine learning context, as it allows efficiently  
 27 processing of data for which a spherical or hyperbolic geometry  
 28 is a natural representation space [BBC<sup>\*</sup>22, BCDC22]. In geom-  
 29 etry processing, a spherical or hyperbolic embedding of geomet-  
 30 rical objects can be at the core of many surface parametrization,  
 31 texture mapping or shape matching problems [HAT<sup>\*</sup>00, GY03,  
 32 GGS03, KSS06, CPS13, BCK18, SCBK20, GSC21]. The challenge  
 33 addressed in this paper is the design of an OT driven sampling  
 34 techniques on Riemannian manifolds with applications to computer  
 35 graphics.

36 **Contributions.** Relying on sliced optimal transport formulation  
 37 for the sphere and the hyperbolic space formulated by Bonet et  
 38 al. [BBC<sup>\*</sup>22, BCDC22], we propose a blue noise sampling strat-  
 39 egy of probability measures on these non-Euclidean spaces. This  
 40 is achieved by providing explicit formulas for the samples advec-  
 41 tion steps and direction pooling in a Riemannian gradient descent  
 42 approach. We then demonstrate the strength of the approach to effi-  
 43 ciently sample meshes through the uniformization theorem allowing  
 44 transforming the intrinsic blue noise sampling problem on the  
 45 mesh, to a blue noise sampling problem in  $\mathbb{S}^2$  or  $\mathbb{H}^2$  depending on  
 46 the mesh topology. We also highlight the interest of the approach  
 47 through projective plane sampling that can be used to sample 3D  
 48 rotations (by sampling quaternions in 4d), as well as various geo-  
 49 metric objects befitting by projective equations (e.g. lines, direc-  
 50 tions...).

## 51 2. Background

52 **Optimal transport.** Given two measures  $\mu$  and  $\nu$ , over some do-  
 53 main  $\Omega$ , and a function  $c(x, y)$  that dictates the cost of moving a  
 54 particle from  $x$  to  $y$  in  $\Omega$ , one can define the Optimal Transport  
 55 problem from  $\mu$  to  $\nu$  as

$$\min_{\pi \in \Pi(\mu, \nu)} \int_{\Omega} c(x, y) d\pi(x, y). \quad (1)$$

56 where  $\Pi(\mu, \nu)$  is the set of couplings:

$$\{\pi \in \mathcal{P}(\Omega \times \Omega), \forall A \subset \Omega, \pi(A \times \Omega) = \mu(A), \pi(\Omega \times A) = \nu(A)\}.$$

57 In most contexts,  $c(x, y) = d^p(x, y)$  where  $d$  is a distance on  
 58  $\Omega$  (e.g. [PC<sup>\*</sup>19]). In such cases we call the minimum cost the  
 59  $p$ -Wasserstein distance between  $\mu$  and  $\nu$ ,  $W_p^p(\mu, \nu)$ . The interest  
 60 of using measures is that its general enough to handle both discrete  
 61 and continuous objects at the same time. Depending on the nature  
 62 of the measures, discrete-to-discrete, semi-discrete, or continuous-  
 63 to-continuous, a huge literature exists on numerical methods to ef-  
 64 ficiently solve OT problems [PC<sup>\*</sup>19, FCG<sup>\*</sup>21].

65 **Sliced Optimal Transport.** Among alternative numerical meth-  
 66 ods, we are interested in fast approximation techniques that scale  
 67 up with the size of the discrete problem and the dimension. First,  
 68 we observe that the one-dimensional OT problem admits the fol-  
 69 lowing closed form solution:

$$W_p^p(\mu, \nu) = \int_0^1 |F_{\mu}^{-1}(u) - F_{\nu}^{-1}(u)|^p du, \quad (2)$$

70 where  $F_{\mu}$  is the cumulative function of the 1D density  $\mu$ , and  $F_{\mu}^{-1}$   
 71 its generalized inverse, or quantile function. For  $p = 1$ , one can  
 72 derive the equivalent formula:

$$W_1(\mu, \nu) = \int_0^1 |F_{\mu}(u) - F_{\nu}(u)| du. \quad (3)$$

73 The transport plan is then simply given by associating the  $i$ th point  
 74 of  $\mu$  to the  $i$ th point of  $\nu$  (see for example [PC<sup>\*</sup>19]) in the case when  
 75  $\mu$  and  $\nu$  are both discrete with the same number of atoms. The ob-  
 76 tained result is the mapping that minimizes the cost to transport  $\mu$   
 77 to  $\nu$ . Hence, a very natural idea is to break a  $d$  dimensional OT  
 78 problem into an infinity of 1 dimensional one. Such an approach  
 79 is referred to as *Sliced Optimal Transport* since it amounts to pro-  
 80 jecting the measures onto 1D slices [PKD05, RPDB11, BRPP15].  
 81 Given a direction  $\theta \in \mathbb{S}^{d-1}$  and the projection  $P^{\theta}(\mathbf{x}) := \langle \mathbf{x}, \theta \rangle$  of  
 82 any  $\mathbf{x} \in \mathbb{R}^d$ , for all  $\mathbf{x} \in \mathbb{R}^d$ , the sliced Wasserstein distance is defined as

$$SW_p^p(\mu, \nu) := \int_{\mathbb{S}^{d-1}} W_p^p(P_{\#}^{\theta} \mu, P_{\#}^{\theta} \nu) d\lambda(\theta), \quad (4)$$

83 where  $P_{\#}^{\theta} \mu$  is the image measure of  $\mu$  by the projection operator.  
 84 The sliced approach receives a lot of attention in the literature as it  
 85 is topologically equivalent to OT [NDC<sup>\*</sup>20] with bounded approx-  
 86 imation of  $W_p$  [Bon13]. On the algorithmic side, the integral over  
 87  $\mathbb{S}^{d-1}$  is obtained used a Monte Carlo approach: we draw random  
 88 directions uniformly on  $\mathbb{S}^{d-1}$  and accumulate 1d Wasserstein dis-  
 89 tances. The computational advantage is that each 1d slice  $W_p^p$  only  
 90 requires to sort the points, leading to an overall computation cost in  
 91  $\mathcal{O}(K \cdot n(d + \log(n)))$  time complexity if  $K$  denotes the number of  
 92 slices used in the Monte Carlo estimation.

93 **Sliced Optimal Transport Sampling (SOTS).** In the context of  
 94 Monte Carlo sampling, Paulin et al. [PBC<sup>\*</sup>20] leveraged the Eu-  
 95 clidean sliced optimal transport formulation to optimize a point  
 96 set such that it better approximates a given target distribution, in  
 97 the sense of the  $SW_2$  metric. In this Monte Carlo rendering setting,  
 98 given a target measure  $\nu$  in  $[0, 1]^d$  (uniform measure for blue noise  
 99 sampling), the objective is to construct  $n$  samples  $\{\mathbf{x}_i\} \in [0, 1]^d$   
 100 defining the discrete distribution  $\mu = \sum_{i=1}^n \delta_{\mathbf{x}_i}$ , such that  $SW_2(\mu, \nu)$   
 101 is minimized. One iteration of the sliced optimal transport sam-  
 102 pling, SOTS for short, algorithm is the following, if  $\mu = \sum_{i=1}^n \delta_{\mathbf{x}_i}$

and if  $v$  is a continuous measure with closed form projection formula on a line (mainly the uniform measure over a ball or a square), we iterate:

$$\mathbf{x}_i^{(K+1)} = \mathbf{x}_i^{(K)} + \frac{\gamma}{L} \sum_{l=1}^L \left( T_l \left( P^{\theta_l}(\mathbf{x}_i^{(K)}) \right) - P^{\theta_l} \left( \mathbf{x}_i^{(K)} \right) \right), \quad (5)$$

where  $T_l$  is the transport plan associated with the solution of the continuous-to-discrete problem between  $P_\#^{\theta_l} v$  and  $P_\#^{\theta_l} \mu$  and  $\gamma > 0$  is a step size (see Fig. 2-left). For the sake of simplicity, the  $P^\theta(\mathbf{x})$  notation refers to the projection of the sample  $\mathbf{x}$  onto the slice  $\theta$  (i.e.  $P_\#^\theta \mu = \sum_i \delta_{P^\theta(\mathbf{x}_i)}$ ). Intuitively, we move each point in the direction of the slice proportionally to the distance to its projected 1d optimal mapping. In [PBC\*20], the authors have demonstrated the interest of such blue noise sampling in  $[0, 1]^d$  for Monte Carlo integration and Monte Carlo rendering. This paper extends this approach to non-Euclidean metric spaces.

**Non-Euclidean Sliced Wasserstein Distance.** Bonet et al. extend the SW distance to Spherical [BBC\*22] and Hyperbolic metric spaces [BCDC22], by replacing the Euclidean notions of lines and projections with the Riemannian equivalent of projection over geodesics. Namely, the spherical geodesics are great-circles of the sphere and geodesics passing through the origin of any hyperbolic model are valid replacements. With these constructions at hand, authors perform various machine learning tasks where the SW distance is generally used as a data fitting loss or a meaningful metric to compare objects defined over such spaces.

**Blue Noise Mesh Sampling.** Blue noise sampling of surfaces in  $\mathbb{R}^3$  is one of our targeted applications. On Euclidean domains, a classical approach to construct well-spread samples in a domain consists in making sure that each pair of samples are separated by at least a given minimum distance. Dart throwing and its variations [Bri07] have naturally been extended to manifolds to achieve such Poisson disk sampling [CJW\*09, BWWM10, Yuk15, GYJZ15]. Alternatively, Voronoi diagrams driven approaches [LWL\*09a, BSD09] and their restriction of discrete manifolds (triangular meshes in most cases), have been used to construct blue noise samples [LWL\*09b, XHGL12, AGY\*17, XLC\*16]. While focusing on remeshing applications, Peyré and Cohen [PC06] have proposed an intrinsic sampling strategy that inserts samples one by one at the location maximizing the (geodesic) distance from the previous samples (approach denoted farthest-point, FP, below). While being efficient from an FMM approximation of the geodesic distance, this algorithm has a greedy approach and is not fit to sample generic non uniform densities. Starting from an initial sampling and pairwise (geodesic) distances between samples, Qin et al. [QCHC17] optimized samples position so that the regularized optimal transport distance between the samples and the uniform measure on the manifold is minimized. Particle based systems can be designed by optimizing the sample distribution on a mesh to uniformize the distances between neighboring samples in ambient space, while staying close to the surface thanks to a projection operator [TMN\*00, ZGW\*13, JZW\*15]. Samples could also be optimized such that they capture the spectral content of the targeted surfaces [ÖAG10]. In most cases, for efficiency purposes, the sampling is performed in ambient space and later projected onto the manifold. While those techniques can be very efficient in terms of

blue noise quality when the mesh embedding to  $\mathbb{R}^3$  is *ambient-compatible* (no too-close sheets of meshes or large enough local shape diameter function [SSCO08], Euclidean unit balls is a good approximation of the geodesic ones...), we propose an efficient purely intrinsic blue noise sampling that can deal with shapes with incorrect embedding (see Fig. 1).

### 3. Sliced optimal transport sampling on constant curvature manifolds

We first extend the SOTS approach defined on Euclidean domains, to the spherical and hyperbolic cases in arbitrary dimensions, respectively denote  $\mathbb{S}^d$  and  $\mathbb{H}^d$  (see Fig. 2).

To define the SOTS in such non-Euclidean spaces, we first need to refine the notion of *projection onto a straight line* as the projection of a set of samples onto geodesic slices for the targeted model (Sec. 3.1). Then we need to solve the matching 1d problem on the geodesic slice (Sec. 3.2). These key ingredients are mostly borrowed from Bonet et al. [BBC\*22, BCDC22] dedicated to the computation of SW on  $\mathbb{S}^d$  and  $\mathbb{H}^d$ . We extend these works with explicit formulas to perform the advection of the samples using group action principle (Sec. 3.3) and Exp and Log maps (Sec. 3.4). Finally, Section 3.5 completes the algorithm describing the extension of the gradient descent of the  $SW_2$  energy. In Section 3.7, we describe a technical improvement of the advection step on batches using a geometric median instead of an average as usually used in SOTS. We summarize the generic algorithm in Alg. 1. Note that we consider a discrete target measure  $v = \sum_{i=1}^m \delta_{y_i}$  with a number of Diracs  $m$  that may be greater than  $n$ . This will be discussed in Section 3.6 to allow the sampling of non-uniform densities. Starting from line 5, we thus solve a balanced optimal transport problem as  $\tilde{v}$  is a random sampling of  $v$  with exactly  $n$  Diracs.

#### 3.1. Geodesic slices and projections

The first step is to find an equivalent to straight lines in the Euclidean space. The most natural choice is a geodesic passing through the origin of the model. In both  $\mathbb{S}^d$  and  $\mathbb{H}^d$  cases, such an object can be obtained by the intersection of a plane with the canonical embedding of each space in  $\mathbb{R}^{d+1}$ .

**Spherical geometry.** As proposed by Bonet et al. [BBC\*22], random slices are defined by the intersection of  $\mathbb{S}^d$  by uniformly sampled Euclidean 2D planes in  $\mathbb{R}^{d+1}$  passing through the origin. This is done by generating two  $(d+1)$ -dimensional vectors with components in  $\mathcal{N}(0, 1)$ , that we orthonormalize (by Gram-Schmidt or Givens rotations). We denote by  $\theta = \{\mathbf{e}_1, \mathbf{e}_2\}$  the two vectors in  $\mathbb{R}^{d+1}$  generated by this process. Such basis of the plane allows defining the projection in  $\mathbb{R}^{d+1}$  onto the associated subspace  $\text{span}(\mathbf{e}_1, \mathbf{e}_2)$ :

$$\Pi^\theta(\mathbf{x}) = \langle \mathbf{x}, \mathbf{e}_1 \rangle \mathbf{e}_1 + \langle \mathbf{x}, \mathbf{e}_2 \rangle \mathbf{e}_2. \quad (6)$$

The projection onto the great circle  $= \text{span}(\mathbf{e}_1, \mathbf{e}_2) \cap \mathbb{S}^d$  becomes

$$P^\theta(\mathbf{x}) := \frac{\Pi^\theta(\mathbf{x})}{\|\Pi^\theta(\mathbf{x})\|}. \quad (7)$$

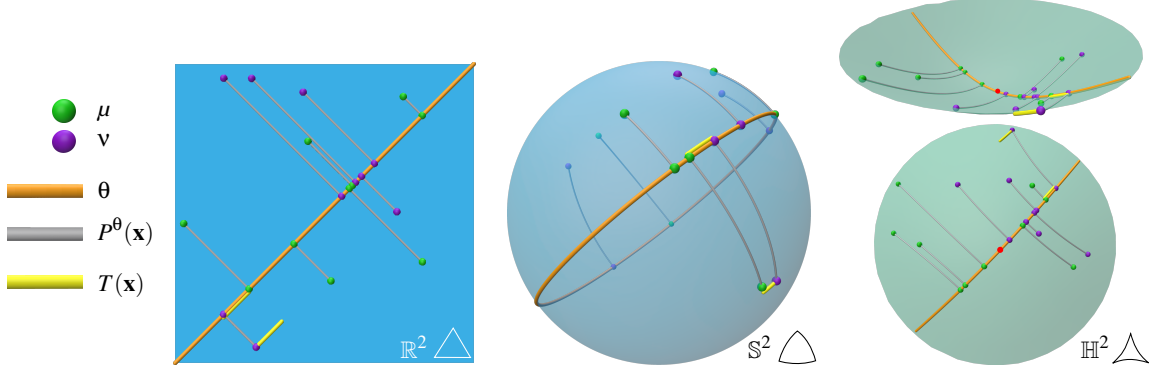


**Figure 2: Sliced optimal transport sampling and notations:** from left to right, on the Euclidean domain (zero curvature metric space), on the spherical one (positive constant curvature metric space), and on the hyperbolic model (Lorentz's model with only a part of the hyperboloid, negative curvature metric space). We only illustrate the assignment and the associated advection for a single sample (yellow bars).

---

**Algorithm 1:** Non Euclidean Sliced Optimal Transport Sampling – NESOTS
 

---

```

Data: The discrete target distribution  $v = \sum_{i=1}^m \delta_{y_i}$ , the number of
iterations  $K$ , the batch size  $L$ , the gradient descent step  $\gamma$ 
Result: The discrete distribution  $\mu^{(K)}$  after  $K$  iterations.
1  $\mu^{(0)} = \text{SubSample}(\tilde{v}, n)$ ; // Init.
2 for  $j \in [[1, K]]$  do
3   parallel for  $l \in [[1, L]]$  do // Batch
4      $\tilde{v} = \text{SubSample}(\tilde{v}, n)$ ; // Sec. 3.6
5      $\theta = \text{RandomSlice}()$ ; // Sec. 3.1
6      $\tilde{v}_\theta = P^\theta(\tilde{v}^l)$ ; // Sec. 3.1
7      $\mu_\theta = P^\theta(\mu^{(j)})$ ; // Sec. 3.1
8      $T = \text{Solve1DOT}(\mu_\theta, \tilde{v}_\theta)$ ; // Sec. 3.2
9     for  $i \in [[1, n]]$  do
10        $\mathbf{g} = \Gamma_\theta(P^\theta(\mathbf{x}_i^{(j)}), T(P^\theta(\mathbf{x}_i^{(j)})))$ ; // Sec. 3.3
11        $\mathbf{d}_i^l = \text{Log}_{\mathbf{x}_i^{(j)}}(\mathbf{g}(\mathbf{x}_i^{(j)}))$ ; // Sec. 3.4
12     end
13   end
14   parallel for  $i \in [[1, n]]$  do
15      $\mathbf{d}_i = \text{GeoMed}(\{\mathbf{d}_i^l\}_L)$ ; // Sec. 3.7
16      $\mathbf{x}_i^{(j+1)} = \text{Exp}_{\mathbf{x}_i^{(j)}}(\gamma \mathbf{d}_i)$ ; // Sec. 3.5
17   end
18 end
19 return  $\mu^{(K)} = \sum_{i=1}^m \delta_{\mathbf{x}_i^{(K)}}$ 
    
```

---

**Hyperbolic geometry.** The  $d$ -dimensional hyperbolic plane  $\mathbb{H}^d$  admits many isometric models (e.g. the Poincaré disk or the Lorentz's hyperboloid models) [Lee06]. For the sake of simplicity of the associated formulas and numerical reasons, we will be using the hyperboloid model, i.e., the upper sheet of the hyperboloid

$$\mathbb{H}^d := \{\mathbf{x} \in \mathbb{R}^{d+1}, \langle \mathbf{x}, \mathbf{x} \rangle_{\mathbb{L}} = -1\},$$

where  $\langle \mathbf{x}, \mathbf{y} \rangle_{\mathbb{L}} := \sum_{i=1}^d x_i y_i - x_{d+1} y_{d+1}$  is the Lorentzian dot product. We denote by  $\mathbf{x}_O$  the origin of the hyperboloid (red dot in Fig. 2), i.e.,  $\mathbf{x}_O = (0, \dots, 0, 1)^t$ . We follow Bonet et al. [BCDC22] by defining the projection on the geodesic obtained as the intersection be-

206 between a 2D plane containing  $\mathbf{x}_O$  and the hyperboloid. The sampling  
 207 of uniform slices is achieved by sampling uniformly the space or-  
 208 thogonal to  $\mathbf{x}_O$ , i.e.  $\mathbf{d} \sim \mathcal{U}(\mathbb{S}^d \times \{0\})$ . We then have the projector

$$P^\theta(\mathbf{x}) := \frac{\Pi^\theta(\mathbf{x})}{\sqrt{-\langle \Pi^\theta(\mathbf{x}), \Pi^\theta(\mathbf{x}) \rangle_{\mathbb{L}}}}, \quad (8)$$

209 where we denote by  $\theta := \{\mathbf{d}, \mathbf{x}_O\}$  the generator of the 2D slice in  
 210  $\mathbb{H}^d$ .

### 3.2. Solving the discrete 1D Wasserstein problem

211 As we will need to evaluate the transport cost on projected sam-  
 212 ples onto the sliced  $\theta$ , we need to clarify the distances between two  
 213 points in  $\mathbb{S}^d$  or  $\mathbb{H}^d$ , and the coordinate on their projection onto  $\theta$ ,  
 214 denoted  $t_\theta(\mathbf{x})$ , the signed geodesic distance to a given origin in  $\theta$ .  
 215

216 **Spherical geometry** On the  $d$ -dimensional unit sphere,  
 217 geodesics are great circles (intersection of a 2-plane passing  
 218 through the origin, and  $\mathbb{S}^d$ ). The geodesic distance between two  
 219 points  $\mathbf{x}, \mathbf{y} \in \mathbb{S}^d$  is simply the angle between the two vectors from  
 220 the origin to the points

$$d_{\mathbb{S}}(\mathbf{x}, \mathbf{y}) := \arccos(\langle \mathbf{x}, \mathbf{y} \rangle). \quad (9)$$

221 As projections lie on a circle, any origin on  $\theta$  can be considered to  
 222 define  $t_\theta$ . If  $\theta = \{\mathbf{e}_1, \mathbf{e}_2\}$ , we use

$$t_\theta(\mathbf{x}) := \frac{\pi + \arctan2(\langle \mathbf{e}_2, \mathbf{x} \rangle, \langle \mathbf{e}_1, \mathbf{x} \rangle)}{2\pi}. \quad (10)$$

223 On  $\mathbb{S}^d$ , the optimal transport problem needs to take into account  
 224 the periodicity of the space, and its associated coordinate systems.  
 225 Fortunately, it can be shown [DRG09] that the problem still boils  
 226 down to a simple sorting of the samples coordinates  $t_\theta$  provided that  
 227 the circle is identified to the Real line through an optimal cut. Find-  
 228 ing the optimal cut can be formulated as a weighted median prob-  
 229 lem, as detailed in Cabrélli et al. [CM98], and admits a  $\mathcal{O}(n \log(n))$   
 230 solution. For some  $\mu, v \in \mathbb{S}^d$  and  $\mathbf{x} \in \mu$ , the map  $T(P^\theta(\mathbf{x}))$  denotes  
 231 the optimal assignment on the slice  $\theta$  of  $\mathbf{x}$  to some  $\mathbf{y} \in v$ .

232 **Hyperbolic geometry** On  $\mathbb{H}^d$ , the geodesic distance between two  
233 points is

$$d_{\mathbb{H}}(\mathbf{x}, \mathbf{y}) := \operatorname{arccosh}(-\langle \mathbf{x}, \mathbf{y} \rangle_{\mathbb{L}}). \quad (11)$$

234 Since the slice is directed by  $\mathbf{d}$ , we define the geodesic distance  
235 coordinate induced by  $\mathbf{d}$

$$t_{\theta}(\mathbf{x}) := \operatorname{sign}(\langle \mathbf{x}, \mathbf{d} \rangle) d_{\mathbb{H}}(\mathbf{x}_O, \mathbf{x}). \quad (12)$$

236 On  $\mathbb{H}^d$ , the optimal assignment is simply obtained by sorting the  
237 projected samples on  $\theta$  and mapping the first projected sample in  
238  $P_{\#}^{\theta} \mu$  to the first one in  $P_{\#}^{\theta} \nu$  (with respect to  $t_{\theta}$ ), similarly to the  
239 Euclidean case.

### 240 3.3. Transitivity and group action

241 In the Euclidean space, samples are advected by a simple trans-  
242 lation in the straight line direction by the distance  $t_{\theta}(\mathbf{x}) -$   
243  $t_{\theta}(T(P^{\theta}(\mathbf{x})))$ . In spherical (Eq. (13)) and hyperbolic (Eq. (14)) do-  
244 mains, we rely on group actions. More precisely, we are interested  
245 in group actions that preserve the geodesics.

246 **Spherical Geometry** The right group to act on the sphere is  
247  $SO(d)$ , i.e., the group of all  $d$ -dimensional rotations. One can build  
248 the rotation that maps a point  $\mathbf{x}$  to a point  $\mathbf{y}$  in  $\mathbb{S}^d$  simply by building  
249 the 2D rotation in their common span,  $\operatorname{span}(\{\mathbf{x}, \mathbf{y}\})$ , i.e.

$$\begin{pmatrix} \cos(\phi) & -\sin(\phi) \\ \sin(\phi) & \cos(\phi) \end{pmatrix}, \quad (275)$$

250 for some  $\phi \in \mathbb{R}$ . To make sure that the part of the vector orthogon-  
251 al to  $\operatorname{span}(\mathbf{x}, \mathbf{y})$  is left unchanged and to avoid building the  $d \times d$   
252 matrix, we decompose any vector  $\mathbf{w}$  in the orthonormal basis given  
253 as the result of the Gram-Schmidt algorithm applied to  $\mathbf{x}$  and  $\mathbf{y}$ .  
254 Leading to

$$\Gamma_{\theta}(\mathbf{x}, \mathbf{y}) : \mathbf{w} \rightarrow \mathbf{w}^{\perp} + \mathbf{x}(\cos(\phi)w_x - \sin(\phi)w_y) + \tilde{\mathbf{y}}(\sin(\phi)w_x + \cos(\phi)w_y), \quad (13)$$

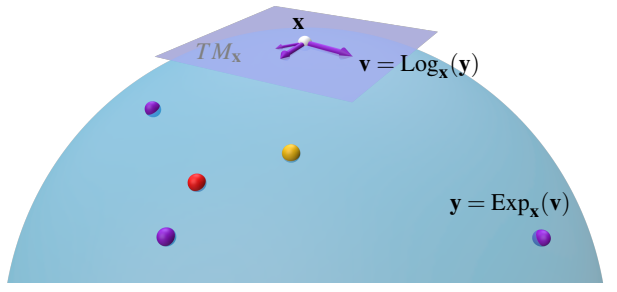
255 where  $\tilde{\mathbf{y}} = \mathbf{y} - \langle \mathbf{x}, \mathbf{y} \rangle \mathbf{x}$ ,  $w_x = \langle \mathbf{w}, \mathbf{x} \rangle$ ,  $w_y = \langle \mathbf{w}, \tilde{\mathbf{y}} \rangle$ ,  $\mathbf{w}^{\perp}$  is the compo-  
256 nent of  $\mathbf{w}$  orthogonal to  $\operatorname{span}(\{e_1, e_2\})$  and  $\phi = d_{\mathbb{S}}(\mathbf{x}, \mathbf{y})$ . One can  
257 verify that we have  $\Gamma_{\theta}(\mathbf{x}, \mathbf{y})(\mathbf{x}) = \mathbf{y}$ . It is also possible to check that  
258 a rotation of  $\phi$  degree along the slice  $\theta$  applied to  $\mathbf{x}$  will offset  $t_{\theta}(\mathbf{x})$   
259 by  $\phi$  (modulo 1). Hence, it is indeed a translation along the slice,  
260 which is the behavior we wanted to translate from the Euclidean  
261 setting.

262 **Hyperbolic Geometry** As a direct analogy, translations along hy-  
263 perbolic slices are hyperbolic rotations, i.e., the elements of the  
264 Lorentz group  $SO_0(d-1, 1)$  (standard rotations preserve the Eu-  
265 clidean scalar product whereas hyperbolic ones preserve  $\langle \cdot, \cdot \rangle_{\mathbb{L}}$ ,  
266 hence the hyperboloid). Computationally, it is very similar to the  
267 spherical case, we want to apply the following 2D rotation in the  
268 span( $\mathbf{x}, \mathbf{y}$ ):

$$\begin{pmatrix} \cosh(\phi) & \sinh(\phi) \\ \sinh(\phi) & \cosh(\phi) \end{pmatrix},$$

269 leading to the analogous decomposition along the right subspaces:

$$\begin{aligned} \Gamma_{\theta}(\mathbf{x}, \mathbf{y}) : \mathbf{w} &\rightarrow \mathbf{w}^{\perp} + \mathbf{d}(\cosh(\phi)w_d + \sinh(\phi)w_0) \\ &\quad + \mathbf{x}_O(\sinh(\phi)w_d + \cosh(\phi)w_0), \end{aligned} \quad (14)$$



270 **Figure 3: Exp and Log maps:** on  $\mathbb{S}^2$ , the orange point is  
271 the point obtained by iteratively going in the average of the  
272  $\log x_{n+1} = \operatorname{Exp}_{x_n}(\frac{\gamma}{n} \sum_i \operatorname{Log}_{x_n}(y_i))$ , which is equivalent to Fréchet  
273 means, whereas the red one is obtained by going in the geometric  
274 median of the directions  $x_{n+1} = \operatorname{Exp}_{x_n}(\gamma \operatorname{GeoMed}(\{\operatorname{Log}_{x_n}(y_i)\}_i))$ .

275 where  $\mathbf{d} = \frac{\Pi_{x_0^{\perp}}(\mathbf{y}-\mathbf{x})}{\|\Pi_{x_0^{\perp}}(\mathbf{y}-\mathbf{x})\|}$ ,  $w_d = \langle \mathbf{w}, \mathbf{d} \rangle$ ,  $w_0 = \langle \mathbf{w}, \mathbf{x}_O \rangle$ ,  $\mathbf{w}^{\perp}$  is the com-  
276 ponent of  $\mathbf{w}$  orthogonal to  $\operatorname{span}(\mathbf{x}_O, \mathbf{d})$  and  $\phi = d_{\mathbb{H}}(\mathbf{x}, \mathbf{y})$ . The only  
277 difference being that we decompose along  $\mathbf{x}_O$  and  $\mathbf{y} - \mathbf{x}$  instead of  
278 directly  $\mathbf{x}$  and  $\mathbf{y}$  (which gives the same span) to make sure that the  
279 points remain on the hyperboloid. We also have  $\Gamma_{\theta}(\mathbf{x}, \mathbf{y})(\mathbf{x}) = \mathbf{y}$ .

### 280 3.4. Exp and Log Maps

281 Beside group actions, Exp and Log maps are key ingredients in Rie-  
282 mannian geometry [Lee06] (see illustration Fig. 3). The  $\operatorname{Exp}_{\mathbf{x}}(\mathbf{v})$   
283 map allows one to follow the geodesic  $\gamma$ , satisfying  $\gamma(0) = \mathbf{x}$  and  
284  $\dot{\gamma}(0) = \mathbf{v} \in TM_{\mathbf{x}}$ , i.e., following the most natural path going from  $\mathbf{x}$   
285 with initial direction and velocity  $\mathbf{v}$  from  $t = 0$  to  $t = 1$ . Conversely,  
286 the  $\operatorname{Log}_{\mathbf{x}}(\mathbf{y}) \in TM_{\mathbf{x}}$  map, the inverse of  $\operatorname{Exp}_{\mathbf{x}}$ , gives the direction  
287 (and velocity) to go from  $\mathbf{x}$  to  $\mathbf{y}$ , i.e.  $\operatorname{Exp}_{\mathbf{x}}(\operatorname{Log}_{\mathbf{x}}(\mathbf{y})) = \mathbf{y}$ . In  $\mathbb{S}^d$  and  
288  $\mathbb{H}^d$ , Exp and Log maps admit closed form expressions.

289 **Spherical geometry.** If  $\Pi_{TM_{\mathbf{x}}}$  denotes the projections from  $\mathbb{R}^d$   
290 onto the tangent space of  $\mathbb{S}^d$  at  $\mathbf{v}$ , we have

$$\operatorname{Exp}_{\mathbf{x}}(\mathbf{v}) = \cos(\|\mathbf{v}\|) \mathbf{x} + \sin(\|\mathbf{v}\|) \frac{\mathbf{v}}{\|\mathbf{v}\|}, \quad (15)$$

$$\operatorname{Log}_{\mathbf{x}}(\mathbf{y}) = \frac{\Pi_{TM_{\mathbf{x}}}(\mathbf{y} - \mathbf{x})}{\|\Pi_{TM_{\mathbf{x}}}(\mathbf{y} - \mathbf{x})\|} d(\mathbf{x}, \mathbf{y}), \quad (16)$$

291 (see Alimisis et al.'s supplemental [ADVA21]).

292 **Hyperbolic geometry.** In the Lorentz hyperbolic model, we have  
293 similar expressions (see e.g. Dai et al. [DWGJ21]):

$$\operatorname{Exp}_{\mathbf{x}}(\mathbf{v}) = \cosh(\|\mathbf{v}\|_{\mathbb{L}}) \mathbf{x} + \sinh(\|\mathbf{v}\|_{\mathbb{L}}) \frac{\mathbf{v}}{\|\mathbf{v}\|_{\mathbb{L}}}, \quad (17)$$

$$\operatorname{Log}_{\mathbf{x}}(\mathbf{y}) = \frac{\operatorname{arccosh}(-\langle \mathbf{x}, \mathbf{y} \rangle_{\mathbb{L}})}{\sqrt{\langle \mathbf{x}, \mathbf{y} \rangle_{\mathbb{L}}^2 - 1}} (\mathbf{y} + \langle \mathbf{x}, \mathbf{y} \rangle_{\mathbb{L}} \mathbf{x}). \quad (18)$$

### 294 3.5. Stochastic Riemannian gradient descent

295 In Euclidean SOTS, when optimizing point sets for blue noise sam-  
296 pling, one can compute a descent direction of the SW energy for

each point by averaging each advection computed for a given number of slices (batch size  $L$  in Alg. 1), hence recovering a mini-batch stochastic gradient descent. On non-Euclidean domains, the advected positions cannot be simply averaged. We propose to use a stochastic Riemannian gradient descent (SRGD) approach combining the gradients obtained in each batch in the tangent plane of each sample [Bou23]. In standard SRGD this would be done by taking the average of the gradients

$$\mathbf{d}_i := \frac{1}{L} \sum_{l=1}^L \mathbf{d}_i^l, \quad (19)$$

but we instead use the geometric median, see 3.7. In our case,  $\mathbf{d}_i^l := \text{Log}_{\mathbf{x}_i^{(j)}}(\mathbf{g}(\mathbf{x}_i^{(j)}))$ , where, following the notations of Alg. 1,  $\mathbf{g}$  is the map that advects the point  $\mathbf{x}_i^{(j)}$  in the  $\theta$  direction following the 1D assignment obtained from the projection onto  $\theta$ . Once the descent direction is computed for each sample, we advect the points using the Exp map by an, exponentially decaying, step size  $\gamma$ :

$$\mathbf{x}_i^{(j+1)} = \text{Exp}_{\mathbf{x}_i^{(j)}}(\gamma \mathbf{d}_i). \quad (20)$$

Note that in the Euclidean setting, this boils down to the original SOTS algorithms [BRPP15] for blue noise sampling in  $[0, 1]^d$ . As a first experiment, Figure 4 compares the blue noise characteristics of the uniform sampling of using NESOTS and classical point patterns on  $\mathbb{S}^2$  [PSC\*15].

### 3.6. Non-uniform densities

When dealing with continuous non-uniform measures  $\phi$  using a sliced approach (e.g. importance sampling Monte Carlo rendering, image stippling), we would first need to have a closed-form formulation of the Radon transform of the target measure of  $\phi$  along the slice  $\theta$ , as discussed Paulin et al. [PBC\*20] for the uniform measure in  $[0, 1]^d$ . To overcome such issue, Salaün et al. [SGSS22] have used a binning strategy of the target points across  $n$  adaptive bins that follow the target distribution. We further simplify this approach on  $\mathbb{S}^d$  and  $\mathbb{H}^d$  using an empirical approximation of  $\phi$  from a discrete measure  $v$  with a large number of samples  $m$  (see Fig. 5). The key idea of Alg. 1 is to start from  $v$  with  $m \gg n$ , and to uniformly pick  $n$  samples from  $v$  at each slice (line 5). As long as  $v \sim \phi$ , this does not affect the minimization of the SW energy, while allowing a lot of flexibility with respect to the applications (see below) and keeping a balanced  $n$ -to- $n$  1d optimal transport problem to solve.

### 3.7. Geometric median

In our experiments, we observe that when targeting non-uniform measures, artifacts may appear during the gradient descent (e.g. alignment of samples as illustrated in Fig. 5-c). Some approaches handle this fact with a more robust advection computation, such as Salaün et al. [SGSS22] but they all require a non-negligible computational overhead, proportional to the input size (for example taking  $m = kn$ ). To overcome this problem without adding limited extra computations, instead of taking the mean of the descent directions, we compute their geometric median. The idea arose from the analogy between the arbitrary bad batches that occurs with poor quality

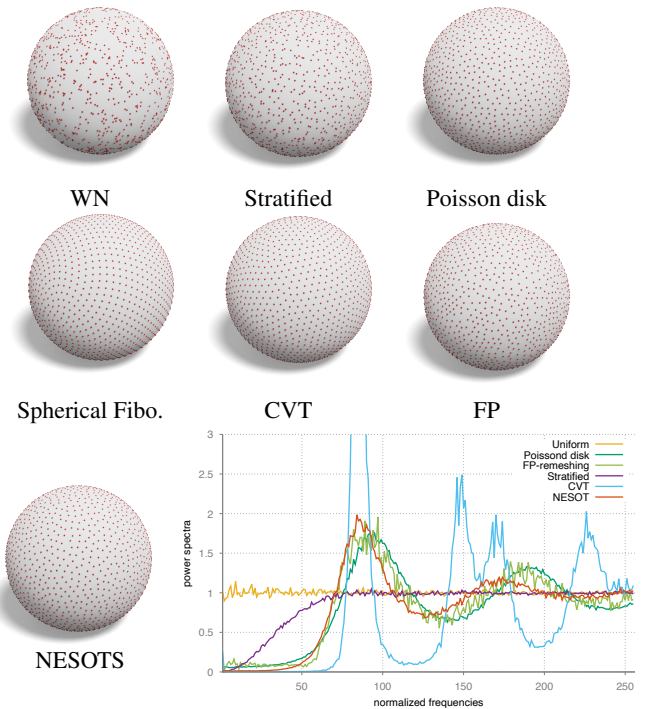


**Figure 4: Blue noise on the sphere.** On  $\mathbb{S}^2$ , we evaluate the blue noise property of our sampling (2048 samples). Our result as to be compared to a uniform sampling, a stratified sampling using a healpix spherical structure [PSC\*15], a Poisson disk sampling, a spherical Fibonacci sequence [KISS15], and a Lloyd's relaxation approach (Centroidal Voronoi Tessellation, CVT) [LWL\*09b], and a geodesic farthest point greedy strategy [PC06] (FP). The graph corresponds to the angular power spectra of the spherical harmonic transform of the point sets (except for spherical Fibonacci whose regular patterns make the spectral analysis less relevant). As discussed in Pilleboue et al. [PSC\*15], our sampler exhibits correct blue noise property with low energy for low frequencies, a peak at the average distance between samples and a plateau with few oscillations for higher frequencies.

subsamples  $\tilde{v}^l$  and malignant voters in voting systems, see [EM-FGH23]. The geometric median can be computed very efficiently, in practice using the Weiszfeld algorithm [Wei37], see Appendix 8.

### 3.8. Real projective plane sampling

A slight modification of the NESOTS algorithm on the sphere allows sampling any density defined on the real projective plane  $\mathbb{P}^d$  in the same blue noise way. Such sampling might have great use in graphics applications since many geometric objects are defined up to signs (such as directing vectors of lines or plane normals). Applications are detailed in section 6.

## 4. Intrinsic discrete manifold sampling

As a first application, we demonstrate the interest of the non-Euclidean sliced optimal transport approach for intrinsic sampling

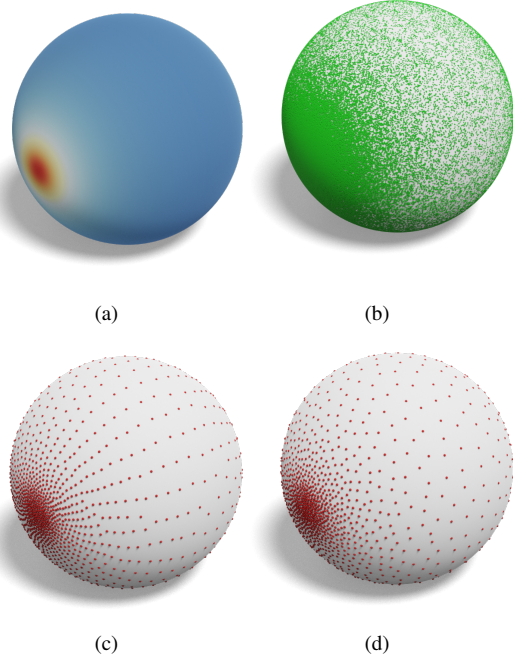


**Figure 5: Non-uniform measure sampling:** given a non-uniform probability measure  $\phi$  in  $S^2$  (a), we first construct a discrete measure  $v \sim \phi$  with a large number of samples, 2048 samples here (b). Figures (c) and (d) are the output of the NESOTS algorithm for 2048 samples ( $L = 32$ ,  $K = 300$ ), when averaging the directions during the advection (c), or using the geometric median (d). While both distributions approximate the density, the latter provides a more stable result without sample alignment artifacts.

of meshes in  $\mathbb{R}^3$ . Given a (closed) mesh  $\mathcal{M}$ , the core idea is to construct an injective map  $\psi$  from  $\mathcal{M}$  to  $S^2$  or  $\mathbb{H}^2$ , to apply NESOTS on these domains to sample the image of the uniform measure  $\mathcal{U}(\mathcal{M})$  on the mesh by  $\psi$  and to pull back the samples onto  $\mathcal{M}$  with  $\psi^{-1}$ . Fig. 6 gives an illustration of this general pipeline.

For surfaces in  $\mathbb{R}^d$ ,  $\psi$  can be built as a conformal map through the uniformization theorem [Abi81]. For short, any Riemannian surface of genus  $g$  admits a constant Gaussian curvature metric: spherical metric if  $g = 0$  ( $S^{d-1}$ , positive constant curvature space), a flat metric if  $g = 1$  ( $\mathbb{R}^{d-1}$ , zero-curvature space) and an hyperbolic metric for  $g \geq 2$  ( $\mathbb{H}^{d-1}$ , negative curvature space). In the discrete setting,  $\mathcal{M}$  and  $\mathcal{M}'$  are discrete conformal equivalent if the edge lengths  $l_{ij}$  and  $l'_{ij}$  are such that  $l'_{ij} = \exp(u_i + u_j)/2 l_{ij}$ , for some conformal factors  $\{u_i\} \in \mathbb{R}$  on vertices [SSP08, BPS15, GLSW18, SCBK20]. In the following, we specifically target the  $g = 0$  and  $g \geq 2$  cases.

Note that in our pipeline, we do not explicitly require the map to be conformal. Any injective map between the mesh and the target space could be considered. We focus here on conformal maps as theoretical guarantees of existence and efficient algorithms to compute them exist. In Fig. 7, we illustrate that comparable blue noise sampling can be obtained non-conformal maps.

In the next section, we describe the sampling algorithm on the sphere, also illustrated in Fig. 6. Section 4.2 focuses on high genus surfaces using an iterated local hyperbolic embedding. Our samples minimize the sliced transport energy to the target measure with respect to the ground metric of the embedded space ( $S^d$  or  $\mathbb{H}^d$ ), not the intrinsic metric of  $\mathcal{M}$ . Yet, from the regularity of the conformal maps we observe that blue noise characteristics are preserved when pulled back from the embedded space to  $\mathcal{M}$  (see Sec. 4.3).

#### 381 4.1. Global spherical embedding

382 The construction of the mapping  $\psi$  through the uniformization theorem depends on the genus  $g$  of  $\mathcal{M}$ . For the sake of simplicity, 383 we start with the spherical case i.e.,  $g = 0$ . By the uniformization 384 theorem, a conformal map exists from  $\mathcal{M}$  to  $S^2$ . Here, we take advantage 385 of the robust tools provided by Gillespie et al. [GSC21] to 386 construct a bijective conformal map  $\psi : \mathcal{M} \rightarrow S^2$ , allowing a global 387 optimization.

---

**Algorithm 2:** Intrinsic Spherical blue noise surface sampling

---

**Data:**  $\mathcal{M}, v, m, n, K, L$  and  $\gamma$  (see Alg. 1)

```

1  $\mathcal{M}_G = \text{BuildMapping}(\mathcal{M}, S^2)$  ;
2  $v_G = \text{sampleMeshFaces}(\mathcal{M}_G, v, m)$  ;
3  $\tilde{\mu}_G = \text{SubSample}(v_G, n)$  ;
4  $\mu_G = \text{NESOTS}(\tilde{\mu}_G, v_G, K, L, \gamma)$  ; // Alg. 1
5  $\mu = \text{MapToMesh}(\mu_G, \mathcal{M}, \mathcal{M}_G)$  ; // Alg. 5
6 return  $\mu$ 
```

---

The global spherical sampling algorithm (Alg. 2) can thus be sketched as follows. For a mesh  $\mathcal{M}$  homeomorphic to the sphere, we first construct  $\psi$  and the global mesh layout  $\mathcal{M}_G$  on  $S^2$ . We then construct the target density  $v_G$  by uniformly sampling  $\mathcal{M}$  with a large number of samples  $m$  (importance sampling of the triangles from the face areas), and projecting the samples onto  $\mathcal{M}_G$ . Note that  $v_G$  is not uniform on the sphere since it captures the distortion induced by  $\psi$ . Finally, we use the NESOTS algorithm to compute the sliced optimal transport sampling  $\mu_G$  and pullback this measure onto the input mesh as described in Sec. 4.3.

#### 399 4.2. Local hyperbolic embedding

If  $\mathcal{M}$  has higher genus, a conformal map exists from  $\mathcal{M}$  to  $\mathbb{H}^2$ . Conformal coefficients can be obtained using the hyperbolic Discrete Yamabe Flow formulation [Luo04, BPS15]. Please refer to Section 4.3 for numerical details. The Yamabe flow allows us to compute the per vertex conformal factors  $\{u_i\}$ , and then the associated (hyperbolic) edge length  $l'_{ij}$  of the embedded mesh  $\mathcal{M}_G$  onto  $\mathbb{H}^2$ . From the updated metric, one can embed  $\mathcal{M}_G$  onto the hyperboloid of the Lorentz model (see Fig 6) using a greedy approach: starting from a initial vertex  $V_0$  set to the origin  $x_O$ , triangles are laid down onto  $\mathbb{H}^2$  in a greedy breadth first strategy process following Schmidt et al.'s approach [SCBK20]. If we continue the BFS visiting the triangles several times, this process reveals that the mapping from  $\mathcal{M}$  to  $\mathbb{H}^2$  is periodic and the conformal map pave the entire hyperbolic plane. This prevents us from duplicating the global approach as described in Section 4.1 since the image of the

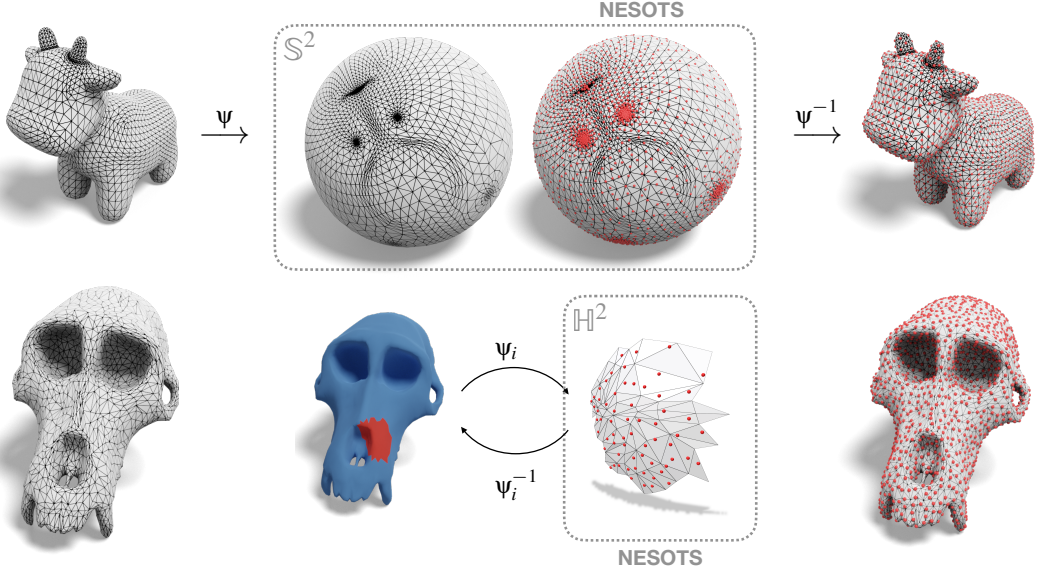


**Figure 6: Overall pipeline of our intrinsic discrete manifold sampling:** starting from an input shape, we conformally embed the discrete structure onto either  $\mathbb{S}^2$  for 0-genus surfaces, or local patches to  $\mathbb{H}^2$  for higher genus one. Then, the NESOTS (Alg. 1) is used (globally or locally) to blue noise sample the embedded structure targeting a measure taking into account the metric distortion.

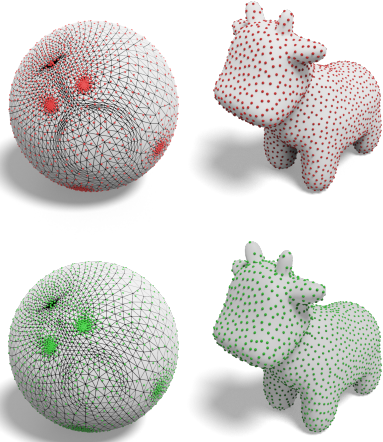


**Figure 7: Sampling using a non-conformal spherical mapping:** first, we recall the NESOTS samplings using CEPS conformal maps (first row). In green, we have updated the mapping using some Laplacian smoothing steps on the sphere, resulting comparable sampling (second row).

422     SOTS on this compact subset of  $\mathbb{H}^2$ . In this process, the choice  
 423     of the first vertex of the layout matters since the distortion will be  
 424     very low in a neighborhood of  $V_0$  (mapped to  $\mathbf{x}_O$ ), and will grow  
 425     exponentially with the distance to it. Hence, using the embedding  
 426     for  $\mathbb{H}^2$  in  $\mathbb{R}^3$ , the main idea of the local algorithm is to construct a  
 427     local layout until the (Euclidean) distance to the origin  $\mathbf{x}_O$ , in the  $z$   
 428     direction, exceeds a certain threshold  $\epsilon$ . As we will ignore triangles  
 429     far from the origin, we only build low distortion mappings. Note  
 430     that the size of the patch for which the distortion is low depends  
 431     on the quality of the mesh (triangle aspect), and on the curvature  
 432     around  $V_0$ . The choice of  $\epsilon$  allows controlling the scale of the op-  
 433     timization, giving a tradeoff between the sliced energy quality and  
 434     speed (smaller patches leads to faster iterations). The effect of  $\epsilon$  is  
 435     evaluated in Fig. 9.

436     When a sample is displaced outside of the patch layout on  $\mathbb{H}^2$ ,  
 437     we just ignore the displacement (similarly to [PBC\*20] when sam-  
 438     pling  $[0, 1]^d$  or the d-Ball). To make sure that all the points are  
 439     optimized as equally as possible, we just keep track of the num-  
 440     ber of times a given vertex  $\mathcal{M}$  has been used as the origin  $v_0$  of  
 441     a patch and iterate on the local patch construction starting by the  
 442     least embedded vertex (the priority queue in Alg. 3). Note that the  
 443     local layout construction is extremely fast (linear complexity in the  
 444     number of triangles of the patch).

445     In Fig. 8, we demonstrate the interest of the intrinsic sampling  
 446     on high genus meshes. When the embedding is ambient-compatible  
 447     (first row), we observe a slightly better sample distribution using  
 448     our approach than FP and Poisson Disk sampling. In contrast, the  
 449     CVT based approach produces a very high quality point pattern.  
 450     Although, when the embedding is defective, our purely intrinsic  
 451     approach led to an almost identical point pattern (in red) when  
 452     mapped back to a better embedding (in blue) (b), whereas both

415 uniform measure  $\mathcal{U}(\mathcal{M})$  by a periodic function is not integrable  
 416 anymore, and hence the Optimal Transport framework cannot be  
 417 used since it is only defined for probability measures.

418 To overcome this problem we restrict the embedding to patches  
 419 of the mesh (see Fig. 6 and Alg. 3): starting from a global Yam-  
 420 abe Flow that is solved only once, we iterate over a local layout  
 421 construction with an associated low distortion map  $\psi_i$ , and use NE-

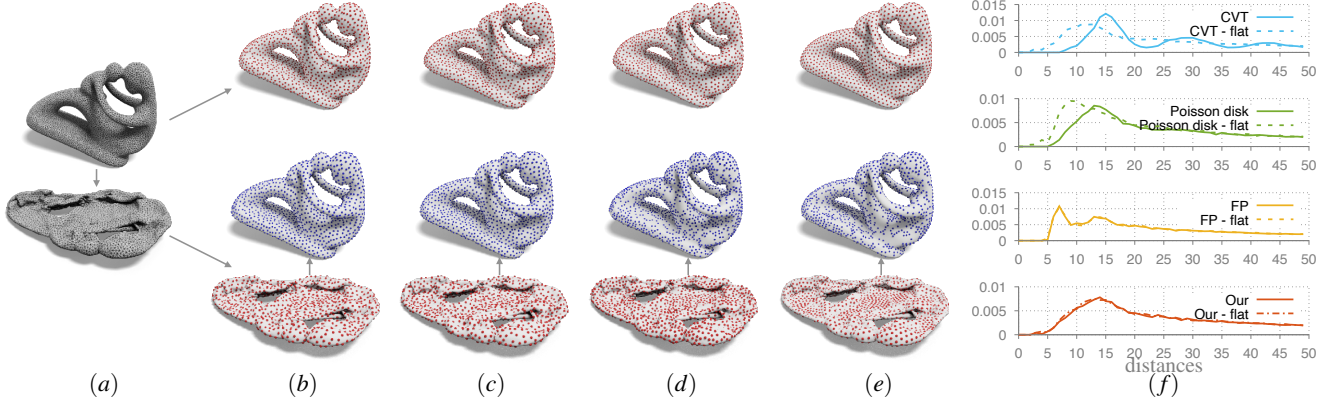


**Figure 8: Intrinsic blue noise sampling of manifolds:** Given the fertility shape with two different Euclidean embeddings (a). The flattened one is obtained through a physical simulation such that the two embeddings are intrinsically isometric. We illustrate the sampling of the meshes with red dots using our approach (b), the intrinsic farthest point approach (FP) [PC06] (c), the Poisson disk sampling in ambient space (d), and the CVT sampling [LWL\*09b] (e). The blue dots correspond to the sampling on the flat embedding that are mapped to the unflattened one. First, we observe that our purely intrinsic approach leads to similar point sets in blue and red in (c). Best point patterns are obtained using CVT when the embedding is correct in  $\mathbb{R}^3$ , i.e. no thin layers ((d)–top). However, for both Poisson disk and CVT, the sampling of the flat embedding leads to defective point patterns (holes in blue samples in (d) and (e)). In (f), we present pair correlation functions for each sampler (both on the flat and top row meshes).

---

**Algorithm 3:** Intrinsic local hyperbolic blue noise surface sampling

---

```

Data:  $\mathcal{M}, \mathbf{v}$  on  $\mathcal{M}$ ,  $n, N, K, L, \gamma, G = \mathbb{H}^2$  (see Alg. 1)
1  $\{u_i\} = \text{YamabeFlow}(\mathcal{M})$  ;
2  $\mathbf{v}_G = \text{sampleMeshFaces}(\mathcal{M}_G, \mathbf{v}, m)$  ;
3 for  $i \in [1, N]$  do
4    $\mathbf{vert} = \text{PopVertexVisitPriorityQueue}()$ ;
5    $(V_i, F_i) = \text{ComputeLocalHyperbolicLayout}(\{u_i\}, \mathbf{vert}, \epsilon)$  ;
6    $\text{UpdateVertexVisitPriorityQueue}(V_i)$ ;
7    $\mu_i = \text{ComputeRestrictionToLayout}(\mu, F_i)$ ;
8    $\mathbf{v}_i = \text{ComputeRestrictionToLayout}(\mathbf{v}, F_i)$ ;
9    $\mu_G = \text{NESOTS}(\mu_i, \mathbf{v}_i, K, L, \gamma)$ ;           // Alg. 1
10   $\mu = \text{MapToMesh}(\mu_G, \mathcal{M}, \mathcal{M}_G)$ ;          // Alg. 5
11 end
12 return  $\mu$ 

```

---

453 Poisson disk and CVT have critical voids and clusters due to bad  
454 assignments. To quantify this finding, we have computed the pair  
455 correlation function (pcf) [IPSS08] the exact geodesic distance on  
456 the manifold between each pair of samples [MMP87]. In Euclidean  
457 domains, pcf and radial mean power spectra capture similar point  
458 pattern characteristics [SÖA\*19]. In Fig. 8-(f), we observe similar  
459 blue noise distribution (a peek at some characteristic distance and  
460 no too-close samples). We also observe that on the flat and non-  
461 flat meshes, our approach leads to similar pcfs. The pcfs CVT and  
462 Poisson disk are highly degraded on the flat geometries. In Fig. 10  
463 we present sampling examples of non-uniform target measures on  
464 meshes. Additional sampling results are given in Fig. 13.

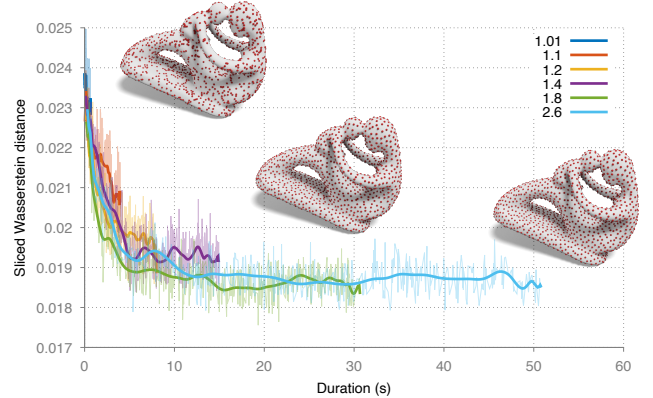


**Figure 9: NESOTS convergence results:** we illustrate the convergence of Alg. 3 using  $N = 500$  iterations ( $K = 500$  and  $L = 32$ ) for 2048 samples, as a function of the  $\epsilon$  parameter. If  $\epsilon$  is too small, local patches are small which implies short timing but low quality blue noise point pattern (as quantified by the SW distance to the uniform measure). As  $\epsilon$  increases, the blue noise quality is improved, but each iteration is longer. For  $\epsilon \in \{1.01, 1.1, 1.2, 1.4, 1.8, 2.6\}$ , the average number of  $\mu_i$  samples in each patch is respectively  $\{3.31, 14.76, 29.97, 61.86, 124.92, 242.82\}$ . Sampled meshes correspond to the final step of  $\epsilon \in \{1.1, 1.4, 2.6\}$  respectively.

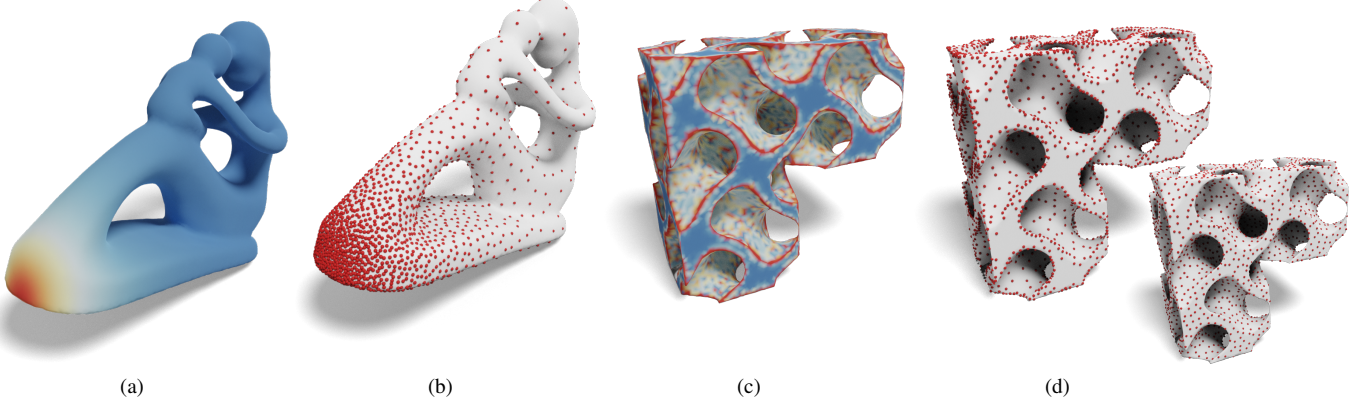


**Figure 10: Non-uniform target density examples on meshes:** given an input probability density function, a smooth one (a) on the `fertility` shape (genus=4 manifold, AIM@shape) and mean curvature driven one in (c) (gyroid surface, genus=32 manifold), our approach is able to generate blue noise samples  $\mu$  approximating the density (2048 samples for (b) and 4096 samples for (d)). In (d) we also illustrate the sampling of the gyroid targeting the uniform density for comparison.

#### 465 4.3. Implementation details and complexity

466 First of all, for the hyperbolic case, discrete conformal coefficients  
 467  $\{u_i\}$  are obtained by minimizing a convex energy, whose gradient  
 468 and Hessian are given in [BPS15]. We thus apply a Newton de-  
 469 scent approach with backtracking to ensure convergence. On the  
 470 models presented in this paper, timings are detailed in Table 1. In  
 471 the spherical case, we rely on the CEPS code provided by Gil-  
 472 lespie et al. [GSC21] to explicitly construct the spherical embedding.  
 473 Once obtained, Alg. 2 is a direct application of Alg. 1 with the same  
 474 computational cost.

475 For the analysis of the local hyperbolic optimization (Alg. 3), we  
 476 experimentally observe that the number of samples  $\mu_i$  and  $v_i$  on the  
 477 layout grows linearly with  $\epsilon$ . If  $C_\epsilon$  denotes the average computation  
 478 cost per slice and per patch, using a batch size  $L$ ,  $K$  steps per patch  
 479 and  $N$  global iterations, we obtain a  $\mathcal{O}(N \cdot K \cdot L \cdot C_\epsilon)$  complexity.  
 480 Note that unless specified otherwise, we have used  $N = 500$ ,  $K =$   
 481  $10$ ,  $\epsilon = 1.5$  and  $L = 32$  for all experiments. Although performances  
 482 were not our primary concern, typical timings are given in Table 1.  
 483 Please refer to Appendix 8 for a discussion on the computational  
 484 cost overhead when using the geometric median instead of simply  
 485 averaging directions in Alg. 1.

486 Once samples are optimized in, either globally for  $\mathbb{S}^2$ , or lo-  
 487 cally for  $\mathbb{H}^2$ , we need an efficient way to retrieve the face of the  
 488 mesh a given sample falls in (and the barycentric coordinates of  
 489 that sample in the face). For that purpose, we exploit the convex-  
 490 ity of the domains: we first construct a BVH of the spherical or  
 491 hyperbolic layout triangles and get the face id by shooting a ray  
 492 through the origin  $(0, 0, 0)$  and the sample (see Alg. 5 in Appendix  
 493 A). Finally, in the hyperbolic case, to avoid having to map all the  
 494  $m$  points of  $\tilde{v}$  on each layout, for each slice, we only map the  
 495  $n$  points that are subsampled from  $\tilde{v}$ . Source code is available at  
 496 <https://github.com/baptiste-genest/NESOTS>.

Shape	Credits	$ V $	$ F $	$g$	Yamabe Flow	NESOTS
spot	[CPS13]	2930	5856	0	n.a.	17.48
duck	deriv. of K. Crane	29999	60006	3	10.67	27.73
fertility	AIM@Shape	8192	16396	4	3.02	15.13
macaca	[WAA*05]	3494	7000	4	1.36	11.12
gyroid	Thingi10k #111246	22115	44354	32	30.37	1.94

**Table 1: Timings.** Mesh statistics and typical timings (in seconds) for the  $g \geq 2$  shapes using the parameters presented in Sec. 4.3 (AMD Ryzen 5000-H, 16 cores).

#### 497 5. Real projective plane $\mathbb{P}^d$ sampling

498 Many objects generated by vectors are defined regardless of their  
 499 length or sign. For instance, the orthographic projection of a 3d  
 500 shape in the direction  $\mathbf{d}$  is the same for all  $\lambda\mathbf{d}, \forall \lambda \neq 0$ . The space  
 501 where collinear vectors are identified is called the Projective Plane  
 502  $\mathbb{P}^d$ . One idea might be to project the points on the sphere, which  
 503 will successfully identify the vectors equivalent up to a positive  
 504 scale  $\lambda > 0$  but not up to a sign. Hence, trying to generate a "uni-  
 505 form" set of lines with any blue noise sampler on the sphere does  
 506 not output satisfactory results as the points are not optimized to  
 507 take into account this equivalence relationship. A simple modifica-  
 508 tion of Alg. 1 described in Alg. 4, allows us to successfully extend  
 509 the blue noise generation of points, in any dimension on  $\mathbb{P}^d$  follow-  
 510 ing any density on the sphere satisfying  $f(\mathbf{x}) = f(-\mathbf{x})$  for  $\mathbf{x} \in \mathbb{S}^d$ .  
 511 To the best of our knowledge, this is new.

512 **Lines and Hyperplanes sampling.** As already stated, lines, char-  
 513 acterized by their unit vector, can be generated uniformly on  $\mathbb{P}^d$   
 514 using Alg. 4 (see Fig. 5 for a 3d blue noise line sampling in  $\mathbb{P}^2$ ). By  
 515 taking the orthogonal complement of such lines, we can similarly  
 516 obtain a blue noise sampling of  $(d - 1)$ -hyperplanes.

517 **Affine line and hyperplane sampling.** Note than even *affine*  
 518 spaces can be sampled by Alg. 4. For instance, an affine line can

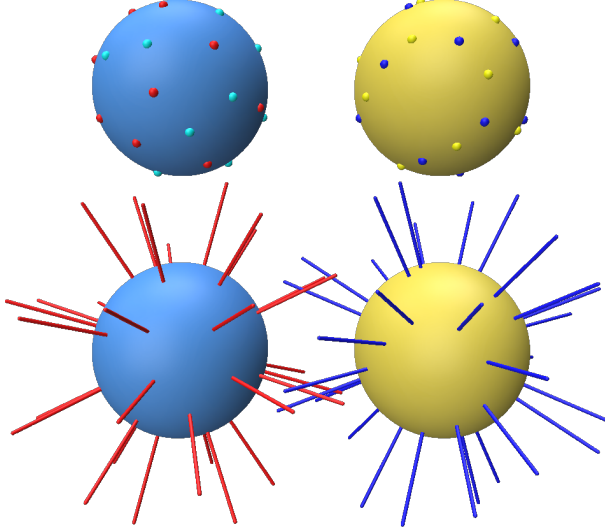


**Figure 11: Projective plane  $\mathbb{P}^2$  sampling:** red points are sampled with Alg. 4, light blue points are the opposites of the red ones. Similarly, blue and yellow points are given by a spherical Fibonacci [KISS15]. Points obtained by Alg. 4 have better blue noise characteristics when considered with their opposites. To illustrate its use, we display at the bottom row the lines generated by the points.

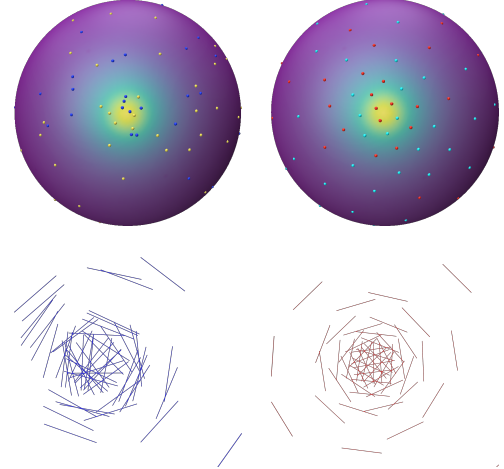


**Figure 12: Affine lines sampling:** from the mapping of lines coefficients to  $\mathbb{P}^2$ , we generate 64 blue noise affine lines following a non-uniform density (top row) using either a white noise sampling (left column) or Alg. 4. When mapped back to  $\mathbb{R}^2$ , our sampling exhibits blue noise characteristics in  $\mathbb{R}^2$  with respect to the metric induced by the Cartesian mapping (second row). Note that here only segments are displayed for the sake of clarity but they are actual lines of  $\mathbb{R}^2$ .

519 described by its Cartesian equation, i.e. in dimension 2

$$ax + by + c = 0, \quad (21)$$

520 but notice that,  $\forall k \neq 0$ , if  $\mathbf{x}$  and  $\mathbf{y}$  are solutions of (21), then  
521  $kax + kby + kc = 0$ . Hence each affine space of dimension  $d$  can  
522 be represented in the projective plane  $\mathbb{P}^d$  by its Cartesian coeffi-  
523 cents (here  $(a, b, c)^t$ ). See Fig. 12 for a 2d affine line sampling  
524 experiment.

525 **Rotation Sampling by Unit Quaternion sampling.** A unit  
526 quaternion  $q$  can act on a vector as a rotation

$$\mathbf{x} \mapsto \mathbf{q}^{-1} \tilde{\mathbf{x}} \mathbf{q},$$

527 where  $\tilde{\mathbf{x}}$  is the imaginary quaternion with  $\mathbf{x}$  as vector part. Since  
528  $\mathbf{q}$  appears twice in the product,  $\mathbf{q}$  and  $-\mathbf{q}$  gives the same rotation.  
529 Hence one can use Alg. 4 on  $\mathbb{P}^3$  to uniformize a set of unit quater-  
530 nions (represented as unit 4 dimensional unit vectors). Previous ap-  
531 proaches such as Alexa’s technique [Ale22], provides good sam-  
532 pling on the 3-Sphere but does not directly tackle the sign equi-  
533 valence problem, which leads to imperfect rotation sampling . The  
534 results of the rotation sampling process is displayed in Fig. 1-(right)  
535 where each shape is rotated by a rotation generated by Alg. 4.

## 536 6. Limitations and future Work

537 Our approach extends the blue noise sampling of any probability  
538 measure through the sliced optimal transport energy, originally de-  
539 signed for Euclidean domains, to Riemannian manifolds: the spher-  
540 ical space  $\mathbb{S}^d$ , the hyperbolic space  $\mathbb{H}^d$ , and the projective one  $\mathbb{P}^d$ .  
541 In a nutshell, from explicit advection and direction averaging steps

---

### Algorithm 4: Real Projective Plane Sampling $\mathbb{P}^d$

---

```

Data:  $\mathbf{v} = \sum_{i=1}^m \delta_{\mathbf{y}_i}$ ,  $K$ ,  $L$ , and  $\gamma$  (see Alg. 1).
Result:  $\mu^{(K)}$ 

1  $\mu^{(0)} = \text{subSample}(\mathbf{v}, 2n)$ 
2 for  $j \in [[1, K]]$  do
3   parallel for  $l \in [[1, L]]$  do                                // Batch
4      $\tilde{\mathbf{v}} = \text{subSample}(\tilde{\mathbf{v}}, 2n)$ ;           // Sec. 3.6
5      $\theta = \text{RandomSlice}()$ ;                   // Sec. 3.1
6      $\tilde{\mathbf{v}}_\theta = P^\theta(\tilde{\mathbf{v}}^l)$ ;             // Sec. 3.1
7      $\mu_\theta = P^\theta(\mu^{(j)}) \cup -P^\theta(\mu^{(j)})$ ; // Sec. 3.1
8      $T = \text{Solve1DOT}(\mu_\theta, \tilde{\mathbf{v}}_\theta)$ ;        // Sec. 3.2
9     for  $i \in [[1, 2n]]$  do
10     $\mathbf{g} = \Gamma_\theta(P^\theta(\mathbf{x}_i^{(j)}), T(P^\theta(\mathbf{x}_i^{(j)})))$ ; // Sec. 3.3
11     $\mathbf{d}_i^l = \text{Log}_{\mathbf{x}_i^{(j)}}(\mathbf{g}(\mathbf{x}_i^{(j)}))$ ;          // Sec. 3.4
12  end
13 end
14 parallel for  $i \in [[1, n]]$  do
15    $\mathbf{d}_i = \text{GeoMed}(\{\mathbf{d}_i^l\}_L \cup \{-\mathbf{d}_{i+n}^l\}_L)$ ; // Sec. 3.7
16    $\mathbf{x}_i^{(j+1)} = \text{Exp}_{\mathbf{x}_i^{(j)}}(\gamma \mathbf{d}_i)$ ;            // Sec. 3.5
17 end
18 end
19 return  $\mu^{(K)} = \sum_{i=1}^m \delta_{\mathbf{x}_i^{(K)}}$ 

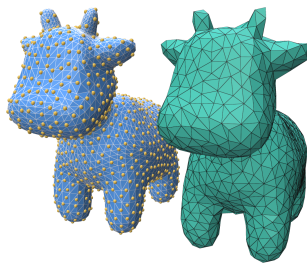
```

---

542 on these spaces, we present a gradient descent strategy that optimizes a point set minimizing the sliced Wasserstein energy. 543

544 First of all, concerning the generic NESOTS approach, there are 545 many opportunities for performance improvements. We are convinced that many variance reduction techniques could be borrowed 546 from Monte Carlo rendering approach to speed up the sliced strategy (e.g. importance sampling of the  $\theta$  directions, control variates 547 using a proxy for the SW energy). 548

550 Thanks to the uniformization theorem, we demonstrated the interest of the approach for intrinsic blue noise sampling of discrete 551 surfaces. Although we may not compete with existing extremely 552 fast restricted Voronoi based techniques when the mesh has a good 553 embedding, we advocate that the purely intrinsic nature of our construction 554 is of interest. An important limitation is the robustness of the global conformal map in the spherical case that may impact 555 the sampling when high distortion occurs. In the hyperbolic case, 556 our local construction mitigates this by controlling potential distortion 557 issues (the  $\varepsilon$  parameter) but we are convinced that improvements 558 exist, e.g. using implicit intrinsic remeshing as in Gillespie et al. [GSC21]. On the geometric side, we only focused  $g = 0$  and 559  $g \geq 2$  surfaces leaving the flat metric space case aside. For  $g = 1$ , 560 cut-and-open strategies must be designed that we avoid in spherical 561 and hyperbolic domains. In this paper, we also focus on the sample 562 generation, leaving the use cases of the point set as future work (e.g. decal placement, function reconstruction, remeshing). 563 For remeshing, the convexity of the  $\mathbb{S}^2$  and  $\mathbb{H}^2$  could be further exploited 564 to reconstruct a mesh: on the  $\mathbb{S}^2$  the convex hull of the optimized samples 565 leads to a trivial (manifold) surface reconstruction (see inset). The hyperbolic case is 566 more complicated as holes could be embedded in a compact subset 567 of  $\mathbb{H}^2$  for which the global convex hull topology does not make sense. We believe that a local combinatorial construction from the convex hull using a small  $\varepsilon$  could be 568 investigated. 569



570 Finally, we have only scratched the use of blue noise sampling 571 in the projective space  $\mathbb{P}^d$  for computer graphics applications. For 572 instance, Monte Carlo-like line and segment sample estimators may 573 lead to drastic reductions of variance in rendering for some effects 574 such as soft shadows or defocusing blur [SMJ17]. We believe that 575 affine line sampling approaches as illustrated in Fig. 12 would be 576 of great interest in this context. 577

## 587 Acknowledgments

588 This research was partially funded by the projects StableProxies 589 (ANR-22-CE46-0006) and OTTOPIA (ANR-20-CHIA-0030) 590 of the French National Research Agency (ANR), and gifts from 591 Adobe Inc. 592

## Appendix A: Additional algorithms

593 The objective of Alg. 5 is to find the face a point is lying on, and to 594 compute the correspondence between its position on the face em-

595 bedded in  $\mathbb{R}^3$  and on the layout in  $\mathbb{S}^2$  (resp  $\mathbb{H}^2$ ) through barycentric 596 coordinates. Even if we theoretically should use spherical (resp. 597 hyperbolic) barycentric coordinates, we observe that the Euclidean 598 barycentric coordinates make a good enough quality proxy while 599 avoiding computing transcendental functions at each mapping. For 600 high performances, the face retrieval can be done leveraging the 601 convexity of  $\mathbb{S}^2$  and  $\mathbb{H}^2$  through a ray shooting approach (rays starting 602 from the domain origin to the sample to locate), with a BVH of the faces. In our implementation, we used the library [PG23]. In

---

### Algorithm 5: Mapping measures between two meshes

```

Data:  $\mu_G$ ,  $\mathcal{M}$  and  $\mathcal{M}_G$ 
1  $\text{BVH} = \text{BuildBVH}(\mathcal{M}_G)$  ;
2 for  $i \in [[1, n]]$  do
3    $\tilde{F} = \text{BVH.intersect}(\mathcal{M}_G, \mathbf{x}_O, \mathbf{x}_i^G)$  ;
4    $b_i = \text{ComputeBarycentricCoordinates}(\mathcal{M}_G, \mathbf{x}_i^G, \tilde{F})$  ;
5    $F = \text{FindCorrespondingFace}(\tilde{F}, \mathcal{M})$  ;
6    $\mathbf{x}_i = \text{PositionFromBarycentricCoordinates}(\mathcal{M}, b_i, F)$  ;
7 end
8 return  $\mu$ 
```

---

603 Alg. 6, we detail the Weiszfeld’s algorithm we use for the geometric 604 median computation using an iterative least squares approach. 605 Note that, as stated in Section 3.7, Weiszfeld’s algorithm is used 606 to combine the gradients (in  $\mathbb{R}^n$ ) during the Riemannian stochastic 607 gradient descent. Theoretically, without the  $\tau$  term, this algorithm

---

### Algorithm 6: Weiszfeld’s geometric median algorithm [Wei37]

```

Data: The samples  $\{\mathbf{x}_i\}_L \in \mathbb{R}^d$ , a stability parameter  $\tau \in \mathbb{R}$ 
1  $\mathbf{y} = \mathbf{0}$  ;
2  $j = 2\tau$  ;
3 while  $j > \tau$  do
4    $d = 0$  ;
5    $w = 0$  ;
6    $\tilde{\mathbf{y}} = \mathbf{0}$  ;
7   for  $i \in [[0, L]]$  do
8      $d = \tau + \|\mathbf{y} - \mathbf{x}_i\|_2$  ;
9      $w += d$  ;
10     $\tilde{\mathbf{y}} += \frac{\mathbf{x}_i}{d}$  ;
11   end
12    $\tilde{\mathbf{y}} /= w$  ;
13    $j = \|\mathbf{y} - \text{next}\|_2$  ;
14    $\mathbf{y} = \tilde{\mathbf{y}}$  ;
15 end
16 return  $\mathbf{y}$ 
```

---

608 does not converge if  $\mathbf{y}_0 = \mathbf{x}_i$  for some  $i$ . In practice, with  $\tau > 0$ , we 609 do not observe convergence issues (interested readers may refer to 610 Cohen et al. [CLM\*16] for a review of standard algorithms). While 611 geometric median is an essential element to guarantee quality of 612 the result for highly non-uniform density functions, a slight com- 613 putational overhead exists when compared to the geometric mean. 614 On the fertility mesh with standard parameters (see Sec 4.3), 615 the optimization part of the Alg. 3 takes 12.38s with the mean and 616 13.33s with the geometric median ( $L = 32$  and  $\tau = 10^{-7}$  for all 617 experiments).

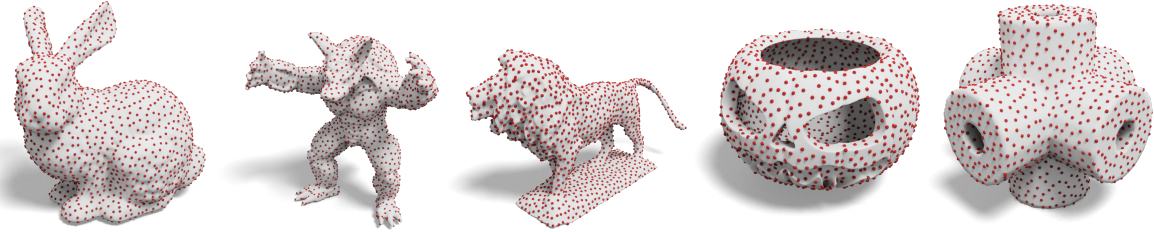


**Figure 13: Intrinsic discrete manifold sampling:** additional sampling results with 2048 samples for  $g = 0$  and  $g \geq 2$  surfaces.

## References

- [Abi81] ABIKOFF W.: The uniformization theorem. *The American Mathematical Monthly* 88, 8 (1981), 574–592. 7
- [ACB17] ARJOVSKY M., CHINTALA S., BOTTOU L.: Wasserstein generative adversarial networks. In *International conference on machine learning* (2017), PMLR, pp. 214–223. 2
- [ADVA21] ALIMISIS F., DAVIES P., VANDEREYCKEN B., ALISTARH D.: Distributed principal component analysis with limited communication. *Advances in Neural Information Processing Systems* 34 (2021), 2823–2834. 5
- [AGY\*17] AHMED A., GUO J., YAN D.-M., FRANCESCHIA J.-Y., ZHANG X., DEUSSEN O.: A simple push-pull algorithm for blue-noise sampling. *Transactions on Visualization and Computer Graphics* 23, 12 (Dec. 2017), 2496–2508. 3
- [Ale22] ALEXA M.: Super-fibonacci spirals: Fast, low-discrepancy sampling of so (3). In *Proceedings of the IEEE/CVF Conference on Computer Vision and Pattern Recognition* (2022), pp. 8291–8300. 11
- [BBC\*22] BONET C., BERG P., COURTY N., SEPTIER F., DRUMETZ L., PHAM M.-T.: Spherical sliced-wasserstein. *arXiv preprint arXiv:2206.08780* (2022). 2, 3
- [BC19] BONNEEL N., COEURJOLLY D.: SPOT: Sliced Partial Optimal Transport. *ACM Trans. Graph.* 38, 4 (July 2019). 2
- [BCDC22] BONET C., CHAPEL L., DRUMETZ L., COURTY N.: Hyperbolic sliced-wasserstein via geodesic and horospherical projections. *arXiv preprint arXiv:2211.10066* (2022). 2, 3, 4
- [BCK18] BADEN A., CRANE K., KAZHDAN M.: Möbius registration. 211–220. 2
- [BD23] BONNEEL N., DIGNE J.: A survey of optimal transport for computer graphics and computer vision. 439–460. 2
- [Bon13] BONNOTTE N.: *Unidimensional and evolution methods for optimal transportation*. PhD thesis, Université Paris Sud-Paris XI; Scuola normale superiore (Pisa, Italie), 2013. 2
- [Bou23] BOUMAL N.: *An introduction to optimization on smooth manifolds*. Cambridge University Press, 2023. 6
- [BPS15] BOBENKO A. I., PINKALL U., SPRINGBORN B. A.: Discrete conformal maps and ideal hyperbolic polyhedra. *Geometry & Topology* 19, 4 (2015), 2155–2215. 7, 10
- [Bri07] BRIDSON R.: Fast poisson disk sampling in arbitrary dimensions. *SIGGRAPH sketches* 10, 1 (2007), 1. 3
- [BRPP15] BONNEEL N., RABIN J., PEYRÉ G., PFISTER H.: Sliced and radon wasserstein barycenters of measures. *Journal of Mathematical Imaging and Vision* 51 (2015), 22–45. 2, 6
- [BSD09] BALZER M., SCHLÖMER T., DEUSSEN O.: Capacity-constrained point distributions: A variant of Lloyd’s method. *ACM Trans. Graph.* 28, 3 (2009), 86:1–8. 3
- [BWWM10] BOWERS J., WANG R., WEI L. Y., MALETZ D.: Parallel poisson disk sampling with spectrum analysis on surfaces. *ACM Transactions on Graphics* 29 (2010). 3
- [CFTR16] COURTY N., FLAMARY R., TUIA D., RAKOTOMAMONY A.: Optimal transport for domain adaptation. *IEEE transactions on pattern analysis and machine intelligence* 39, 9 (2016), 1853–1865. 2
- [CJW\*09] CLINE D., JESCHKE S., WHITE K., RAZDAN A., WONKA P.: Dart throwing on surfaces. In *Computer Graphics Forum* (2009), vol. 28, Wiley Online Library, pp. 1217–1226. 3
- [CLM\*16] COHEN M. B., LEE Y. T., MILLER G., PACHOCKI J., SIDFORD A.: Geometric median in nearly linear time. In *Proceedings of the forty-eighth annual ACM symposium on Theory of Computing* (2016), pp. 9–21. 12
- [CM98] CABRELLI C. A., MOLTER U. M.: A linear time algorithm for a matching problem on the circle. *Information processing letters* 66, 3 (1998), 161–164. 4
- [CPS13] CRANE K., PINKALL U., SCHRÖDER P.: Robust fairing via conformal curvature flow. *ACM Transactions on Graphics (TOG)* 32, 4 (2013), 1–10. 2, 10
- [DGBOD12] DE GOES F., BREEDEN K., OSTROMOUKHOV V., DESBRUN M.: Blue noise through optimal transport. *ACM Trans. Graph.* 31, 6 (2012), 171. 2
- [DRG09] DELON J., RABIN J., GOUSSEAU Y.: Transportation distances on the circle and applications. *arXiv preprint arXiv:0906.5499* (2009). 4
- [DWGJ21] DAI J., WU Y., GAO Z., JIA Y.: A hyperbolic-to-hyperbolic graph convolutional network. In *Proceedings of the IEEE/CVF Conference on Computer Vision and Pattern Recognition* (2021), pp. 154–163. 5
- [EMFGH23] EL-MHAMDI E.-M., FARHADKHANI S., GUERRAOUI R., HOANG L.-N.: On the strategyproofness of the geometric median. In *International Conference on Artificial Intelligence and Statistics* (2023), PMLR, pp. 2603–2640. 6
- [FCG\*21] FLAMARY R., COURTY N., GRAMFORT A., ALAYA M. Z., BOISBUNON A., CHAMBON S., CHAPEL L., CORENFLOS A., FATRAS K., FOURNIER N., GAUTHERON L., GAYRAUD N. T., JANATI H., RAKOTOMAMONY A., REDKO I., ROLET A., SCHUTZ A., SEGUY V., SUTHERLAND D. J., TAVENARD R., TONG A., VAYER T.: Pot: Python optimal transport. *Journal of Machine Learning Research* 22, 78 (2021), 1–8. 2
- [GGS03] GOTSMAN C., GU X., SHEFFER A.: Fundamentals of spherical parameterization for 3d meshes. In *ACM SIGGRAPH 2003 Papers*. 2003, pp. 358–363. 2
- [GLSW18] GU X. D., LUO F., SUN J., WU T.: A discrete uniformization theorem for polyhedral surfaces. *Journal of differential geometry* 109, 2 (2018), 223–256. 7
- [GSC21] GILLESPIE M., SPRINGBORN B., CRANE K.: Discrete conformal equivalence of polyhedral surfaces. *ACM Trans. Graph.* 40, 4 (2021). 2, 7, 10, 12
- [GY03] GU X., YAU S.-T.: Global conformal surface parameterization. In *Proceedings of the 2003 Eurographics/ACM SIGGRAPH symposium on Geometry processing* (2003), pp. 127–137. 2
- [GYJZ15] GUO J., YAN D.-M., JIA X., ZHANG X.: Efficient maximal

- 716    poisson-disk sampling and remeshing on surfaces. *Computers & Graphics* 717 46 (2015), 72–79. 3
- 718    [HAK\*00] HAKER S., ANGENENT S., TANNENBAUM A., KIKINIS R., 719 SAPIRO G., HALLE M.: Conformal surface parameterization for texture 720 mapping. *IEEE Transactions on Visualization and Computer Graphics* 721 6, 2 (2000), 181–189. 2
- 722    [HGK\*16] HUANG G., GUO C., KUSNER M. J., SUN Y., SHA F., 723 WEINBERGER K. Q.: Supervised word mover's distance. *Advances* 724 *in neural information processing systems* 29 (2016). 2
- 725    [IPSS08] ILLIAN J., PENTTINEN A., STOYAN H., STOYAN D.: *Statistical* 726 *analysis and modelling of spatial point patterns*. John Wiley & Sons, 727 2008. 9
- 728    [JZW\*15] JIANG M., ZHOU Y., WANG R., SOUTHERN R., ZHANG 729 J. J.: Blue noise sampling using an sph-based method. *Transactions* 730 *on Graphics* 34, 6 (2015), 1–11. 3
- 731    [KISS15] KEINERT B., INNMANN M., SÄNGER M., STAMMINGER M.: 732 Spherical fibonacci mapping. *ACM Transactions on Graphics (TOG)* 733 34, 6 (2015), 1–7. 6, 11
- 734    [KSS06] KHAREVYCH L., SPRINGBORN B., SCHRÖDER P.: Discrete 735 conformal mappings via circle patterns. *ACM Transactions on Graphics* 736 *(TOG)* 25, 2 (2006), 412–438. 2
- 737    [Lee06] LEE J. M.: *Riemannian manifolds: an introduction to curvature*, 738 vol. 176. Springer Science & Business Media, 2006. 4, 5
- 739    [Luo04] LUO F.: Combinatorial Yamabe flow on surfaces. *Communications* 740 *in Contemporary Mathematics* 6, 05 (2004), 765–780. 7
- 741    [LWL\*09a] LIU Y., WANG W., LÉVY B., SUN F., YAN D.-M., LU L., 742 YANG C.: On centroidal voronoi tessellation, energy smoothness and 743 fast computation. *Transactions on Graphics* 28, 4 (08 2009), 1–17. 3
- 744    [LWL\*09b] LIU Y., WANG W., LÉVY B., SUN F., YAN D.-M., LU L., 745 YANG C.: On centroidal voronoi tessellation—energy smoothness and 746 fast computation. *ACM Transactions on Graphics (ToG)* 28, 4 (2009), 747 1–17. 3, 6, 9
- 748    [MMP87] MITCHELL J. S., MOUNT D. M., PAPADIMITRIOU C. H.: 749 The discrete geodesic problem. *SIAM Journal on Computing* 16, 4 750 (1987), 647–668. 9
- 751    [NDC\*20] NADJAHI K., DURMUS A., CHIZAT L., KOLOURI S., 752 SHAHRAPOUR S., SIMSEKLI U.: Statistical and topological properties 753 of sliced probability divergences. *Advances in Neural Information* 754 *Processing Systems* 33 (2020), 20802–20812. 2
- 755    [NG18] NADER G., GUENNEBAUD G.: Instant transport maps on 2d 756 grids. *ACM Trans. Graph.* 37, 6 (2018), 13. 2
- 757    [ÖAG10] ÖZTIRELI C., ALEXA M., GROSS M.: Spectral sampling of 758 manifolds. *ACM Transactions on Graphics (TOG)* 29, 6 (2010), 1–8. 3
- 759    [PBC\*20] PAULIN L., BONNEEL N., COEURJOLLY D., IEHL J.-C., 760 WEBANCK A., DESBRUN M., OSTROMOUKHOV V.: Sliced optimal 761 transport sampling. *ACM Trans. Graph.* 39, 4 (2020), 99. 2, 3, 6, 8
- 762    [PC06] PEYRÉ G., COHEN L. D.: Geodesic remeshing using front propagation. *International Journal of Computer Vision* 69 (2006), 145–156. 763 3, 6, 9
- 764    [PC\*19] PEYRÉ G., CUTURI M., ET AL.: Computational optimal 765 transport: With applications to data science. *Foundations and Trends® in* 766 *Machine Learning* 11, 5–6 (2019), 355–607. 2
- 767    [PG23] PÉRARD-GAYOT A.: BVH construction and traversal library, 768 2023. URL: <https://github.com/madmann91/bvh>. 12
- 769    [PKD05] PITIÉ F., KOKARAM A. C., DAHYOT R.: N-dimensional prob- 770 ability density function transfer and its application to colour transfer. In 771 *IEEE Int. Conf. on Computer Vision (ICCV)* (2005). 2
- 772    [PSC\*15] PILLEBOUE A., SINGH G., COEURJOLLY D., KAZHDAN M., 773 OSTROMOUKHOV V.: Variance analysis for monte carlo integration. 774 *ACM Trans. Graph. (Proc. SIGGRAPH)* 34, 4 (2015), 124:1–124:14. 6
- 775    [QCHC17] QIN H., CHEN Y., HE J., CHEN B.: Wasserstein blue noise 776 sampling. *ACM Transactions on Graphics (TOG)* 36, 5 (2017), 1–13. 2, 777 3
- 778    [RPDB11] RABIN J., PEYRÉ G., DELON J., BERNOT M.: Wasserstein 779 barycenter and its application to texture mixing. In *International Conference* 780 *on Scale Space and Variational Methods in Computer Vision* (2011), Springer, pp. 435–446. 2
- 781    [SCBK20] SCHMIDT P., CAMPEN M., BORN J., KOBELT L.: Inter- 782 surface maps via constant-curvature metrics. *ACM Transactions on* 783 *Graphics (TOG)* 39, 4 (2020), 119–1. 2, 7
- 784    [SdGP\*15] SOLOMON J., DE GOES F., PEYRÉ G., CUTURI M., 785 BUTSCHER A., NGUYEN A., DU T., GUIBAS L.: Convolutional 786 wasserstein distances: Efficient optimal transportation on geometric 787 domains. *ACM Trans. Graph.* 34, 4 (2015), Art. 66. 2
- 788    [SGSS22] SALAÜN C., GEORGIEV I., SEIDEL H.-P., SINGH G.: Scal- 789 able multi-class sampling via filtered sliced optimal transport. *arXiv* 790 preprint [arXiv:2211.04314](https://arxiv.org/abs/2211.04314) (2022). 2, 6
- 791    [SMJ17] SINGH G., MILLER B., JAROSZ W.: Variance and convergence 792 analysis of Monte Carlo line and segment sampling. *Computer Graphics* 793 *Forum (Proceedings of EGSR)* 36, 4 (June 2017). 12
- 794    [SÖA\*19] SINGH G., ÖZTIRELI C., AHMED A. G., COEURJOLLY D., 795 SUBR K., DEUSSEN O., OSTROMOUKHOV V., RAMAMOORTHI R., 796 JAROSZ W.: Analysis of sample correlations for monte carlo rendering. 797 473–491. 2, 9
- 798    [SRGB14] SOLOMON J., RUSTAMOV R., GUIBAS L., BUTSCHER A.: 799 Earth mover's distances on discrete surfaces. *ACM Trans. Graph.* 33, 4 800 (2014), Art. 67. 2
- 801    [SSCO08] SHAPIRA L., SHAMIR A., COHEN-OR D.: Consistent mesh 802 partitioning and skeletonisation using the shape diameter function. *The* 803 *Visual Computer* 24 (2008), 249–259. 3
- 804    [SSP08] SPRINGBORN B., SCHRÖDER P., PINKALL U.: Conformal 805 equivalence of triangle meshes. In *ACM SIGGRAPH 2008 papers*. 2008, 806 pp. 1–11. 7
- 807    [TMN\*00] TANAKA S., MORISAKI A., NAKATA S., FUKUDA Y., 808 YAMAMOTO H.: Sampling implicit surfaces based on stochastic differential 809 equations with converging constraint. *Computers & Graphics* 24, 3 810 (2000), 419–431. 3
- 811    [V\*09] VILLANI C., ET AL.: *Optimal transport: old and new*, vol. 338. 812 Springer, 2009. 1
- 813    [WAA\*05] WILEY D. F., AMENTA N., ALCANTARA D. A., GHOSH 814 D., KIL Y. J., DELSON E., HARCOURT-SMITH W., ROHLF F. J., 815 ST JOHN K., HAMANN B.: *Evolutionary morphing*. IEEE, 2005. 10
- 816    [Wei37] WEISZFELD E.: Sur le point pour lequel la somme des distances 817 de  $n$  points donnés est minimum. *Tohoku Mathematical Journal, First* 818 *Series* 43 (1937), 355–386. 6, 12
- 819    [XHGL12] XU Y., HU R., GOTSMAN C., LIU L.: Blue noise sampling 820 of surfaces. *Computers & Graphics* 36, 4 (2012), 232–240. 3
- 821    [XLC\*16] XIN S.-Q., LÉVY B., CHEN Z., CHU L., YU Y., TU C., 822 WANG W.: Centroidal power diagrams with capacity constraints: Com- 823 putation, applications, and extension. *Transactions on Graphics* 35, 6 824 (2016), 1–12. 3
- 825    [Yuk15] YUKSEL C.: Sample elimination for generating poisson disk 826 sample sets. In *Computer Graphics Forum* (2015), vol. 34, Wiley Online 827 Library, pp. 25–32. 3
- 828    [ZGW\*13] ZHONG Z., GUO X., WANG W., LÉVY B., SUN F., LIU Y., 829 MAO W., ET AL.: Particle-based anisotropic surface meshing. *Transac-* 830 *tions on Graphics* 32, 4 (2013), 99–1. 3
- 831    [832]